

MASARYKOVA UNIVERZITA
PŘÍRODOVĚDECKÁ FAKULTA
ÚSTAV TEORETICKÉ FYZIKY A ASTROFYZIKY

Bakalářská práce

BRNO 2022

MATĚJ BÁRTA

M A S A R Y K O V A
U N I V E R Z I T A
PŘÍRODOVĚDECKÁ FAKULTA
ÚSTAV TEORETICKÉ FYZIKY A ASTROFYZIKY

Galaxy evolution with ALMA - Effects of ram pressure stripping on the kinematics of cluster galaxies

Bakalářská práce

Matěj Bárta

Vedoucí práce: Mgr. Pavel Jáchym Ph.D. Brno 2022

Bibliografický záznam

Autor: Matěj Bárta
Přírodovědecká fakulta, Masarykova univerzita
Ústav teoretické fyziky a astrofyziky

Název práce: Galaxy evolution with ALMA - Effects of ram pressure stripping on the kinematics of cluster galaxies

Studijní program: B-FYZ Fyzika

Studijní obor: ASTRO Astrofyzika

Vedoucí práce: Mgr. Pavel Jáchym Ph.D.

Akademický rok: 2021/2022

Počet stran: ix + 40

Klíčová slova: kupa galaxií; ALMA; ESO137-001; medúzovitá galaxie; 3D-Barolo; kupa v Pravítku; evoluce galaxií; kinematika galaxií

Bibliographic Entry

Author: Matěj Bárta
Faculty of Science, Masaryk University
Department of theoretical physics and astrophysics

Title of Thesis: Galaxy evolution with ALMA - Effects of ram pressure stripping on the kinematics of cluster galaxies

Degree Programme: B-FYZ Physics

Field of Study: ASTRO Astrophysics

Supervisor: Mgr. Pavel Jáchym Ph.D.

Academic Year: 2021/2022

Number of Pages: ix + 40

Keywords: Galaxy cluster; ALMA; ESO137-001; jellyfish galaxy; 3D-Barolo; Norma cluster; galaxy evolution; galaxy kinematics

Abstrakt

Evoluce galaxie je silně ovlivněna působením okolního prostředí. Tato práce se zabývá působením dynamického tlaku na galaxii ESO137-001 pohybující se hustým prostředím uvnitř kupy galaxií v souhvězdí Právítka. Využili jsme detailních pozorování emisní čáry CO(2-1) pořízené pomocí radioteleskopu ALMA, trasující rozložení molekulárního plynu. Vizualizace efektu byla vytvořena použitím několika metod široce používaných pro studium kinematiky galaxií. Mapa integrované intenzity (moment 0) ukazuje asymetrické rozložení molekulárního plynu v centrálních částech galaxie. Vytvořené diagramy závislosti rychlosti na pozici podél dané oblasti vykazují struktury běžné pro spirální galaxie, jsou ovšem narušené působením vnějšího dynamického tlaku. Odečet hvězdného disku od CO dat odhalil regiony nejvíce ovlivněné vnějším tlakem.

Abstract

The galactic evolution is greatly affected by the surrounding environment. This thesis explores effects of ram pressure stripping (RPS) on the galaxy ESO137-001 as it is moving through the dense intra-cluster medium of the Norma cluster. We used detailed observations of the CO(2-1) emission line made by ALMA, tracing the distribution of molecular gas in the galaxy. Visualization of the effects was produced by implementing several methods widely used to study galactic kinematics. Integrated flux map shows asymmetric distribution of the molecular gas confined in the inner-most regions of the galaxy. Created position-velocity diagrams exhibit structures typical for spiral galaxies, however perturbed by the RPS. Subtraction of the stellar disc from the CO observations revealed the most affected regions by the RPS.

ZADÁNÍ
BAKALÁŘSKÉ PRÁCE

Akademický rok: 2021/2022

Ústav:	Ústav teoretické fyziky a astrofyziky
Student:	Matěj Bárta
Program:	Fyzika
Specializace:	Astrofyzika

Ředitel ústavu PŘF MU Vám ve smyslu Studijního a zkušebního řádu MU určuje bakalářskou práci s názvem:

Název práce:	Galaxy evolution with ALMA - Effects of ram pressure stripping on the kinematics of cluster galaxies
Název práce anglicky:	Galaxy evolution with ALMA - Effects of ram pressure stripping on the kinematics of cluster galaxies
Jazyk závěrečné práce:	angličtina

Oficiální zadání:

Milimetrová a sub-milimetrová interferometrická observatoř ALMA je jedinečným a špičkovým zařízením pro astronomický výzkum především chladných oblastí ve vesmíru. Od svého vzniku má na kontě mnoho průlomových objevů. Navrhovaná práce je zaměřena na teoretické a praktické seznámení se s principy milimetrové interferometrie a na zpracování a analýzu dat. Praktická aplikace bude probíhat s daty z archivu ALMA. Jedná se o pozorování CO záření v galaxii ESO137-001 v kupě galaxií Norma. Tato galaxie je jedním z nejdůležitějších příkladů tzv. ram-pressure stripped (RPS) galaxií, ze kterých je působením vnějšího dynamického tlaku okolního horkého plynu (mezigalaktického prostředí, ICM) odstraňována jejich mezihvězdná hmota (ISM). Analýza dat se zaměří na zkoumání kinematiky disku ESO137-001, která doposud nebyla podrobně zkoumána. Působením vnějšího tlaku je symetrický rotační pohyb v disku galaxie silně narušen. Z dat budou vytvořeny a studovány mapy rychlostního rozložení a rozložení disperze rychlostí (momenty 1 a 2) a také position-velocity diagramy (PVD) podél hlavní osy galaxie. Také bude vytvořen model rotujícího disku, který bude následně odečten od dat. Tím se získá reziduální mapa/datová kostka, ve které bude možné sledovat nekruhové složky rychlosti v disku a zkoumat příčiny jejich vzniku.

Vedoucí práce:	Mgr. Pavel Jáchym, Ph.D.
Datum zadání práce:	18. 11. 2021
V Brně dne:	28. 1. 2022

Zadání bylo schváleno prostřednictvím IS MU.

Matěj Bárta, 15. 12. 2021

Mgr. Pavel Jáchym, Ph.D., 12. 1. 2022

RNDr. Luboš Poláček, 14. 1. 2022

Poděkování

Tímto bych chtěl především poděkovat svému vedoucímu Mgr. Pavlu Jáchymovi, PhD za trpělivost, odborné vedení a cenné rady při vypracovávání této práce. Také bych chtěl touto cestou poděkovat své rodině a přátelům, kteří mě podporovali během celé doby studia.

Prohlášení

Prohlašuji, že jsem svoji bakalářskou práci vypracoval samostatně pod vedením vedoucího práce s využitím informačních zdrojů, které jsou v práci citovány.

Brno 23. května 2022

.....
Matěj Bárta

Contents

Used acronyms	ix
Introduction	1
Chapter 1. Radio astronomy	2
1.1 Electromagnetic spectrum	2
1.1.1 Radio and microwave radiation	2
1.2 Apertures synthesis	3
1.2.1 Basic principles	4
1.3 Atacama Large Millimeter/submillimeter Array	4
1.3.1 Technical information	4
Chapter 2. Ram pressure stripping	6
2.1 Physical process	6
2.2 Observable impact on galaxy	7
2.3 Impact on galaxy evolution	8
Chapter 3. The galaxy ESO137-001	9
Chapter 4. Data processing	12
4.1 Software	12
4.2 Used data	12
4.3 Data preparation	13
4.4 Moment maps	13
4.5 Disc center	16
4.6 Position-velocity diagrams	17
4.6.1 Linear regions	17
4.6.2 PVDs along principal axes	17
4.6.3 Offset PVDs	20
4.6.4 Comparison with stellar disc	22
4.7 Fitting rotating stellar disc	24
4.8 Residual velocity map	25
Conclusions	28

Appendix	29
A Figures - Effect of averaging width on PVD	29
B Parallel line region generator function	30
C PVD generator function	35
Bibliography	39

Used acronyms

ALMA	Atacama Large Millimeter/submillimeter Array
FWHM	Full width at half maximum
HST	Hubble Space Telescope
ICM	Intra-cluster medium
ISM	Interstellar medium
MUSE	Multi Unit Spectroscopic Explorer
PVD	Position-velocity diagram
RPS	Ram Pressure Stripping
VLT	Very Large Telescope
WCS	World Coordinate System

Introduction

The largest gravitationally bound objects in the universe are galaxy clusters. They usually contain hundreds to thousands of member galaxies orbiting around a common point - the clusters center of gravity. Together with galaxies, galaxy clusters contain large fraction of hot and dense ionized gas – the intra-cluster medium (ICM).

Galaxies travel through the cluster at high speeds of order of $100\text{-}1000\text{ km s}^{-1}$. Interaction with the surrounding ICM creates ram pressure which can tear away gaseous components of the galaxy disc, sometimes creating long galactic tails resembling those of comets. Removal of gas from the galaxy results in rapid decrease in star formation, practically 'killing' the host galaxy. On the other hand, these tails full of gas can accommodate new star-forming clouds.

Galactic tails were observed through nearly the whole electromagnetic spectrum, most recently in radio and millimeter waves. With the use of radio interferometers, we are able to observe this phenomena in details never achieved before. These new radio observations of the cold atomic and molecular gas are uncovering new details of the interaction and its effect on the galactic evolution.

In the first part of this thesis, we will briefly introduce both concepts - Radio interferometry and Ram-pressure stripping. In the second part, we will take detailed ALMA observations of one such 'jellyfish' galaxy and investigate the effect of RPS on the molecular component of its disc as it is being torn away from its galactic parent.

Chapter 1

Radio astronomy

When Karl G. Jansky in the year 1931 did the 'impossible' and detected extraterrestrial radio signal, new 'window' into the cosmos was opened. From the times of Jansky, many astrophysicists continued to carefully listen to the cosmic radio stations.

1.1 Electromagnetic spectrum

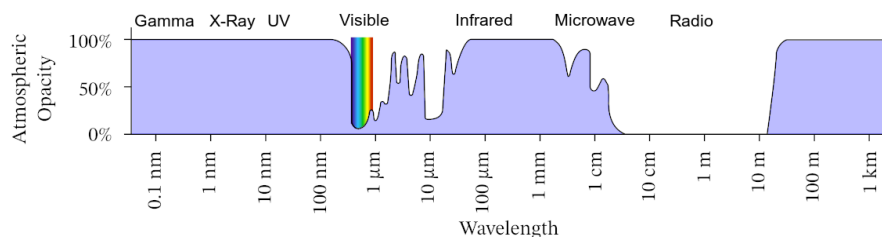


Figure 1.1: Electromagnetic spectrum

In 1860s J. C. Maxwell developed partial differential equations indicating possible waves in the electromagnetic field. For the supposed electromagnetic waves, the equations predicted infinite range of frequencies with constant travel speed known as the speed of light. This led Maxwell to conclude that visible light is an electromagnetic wave that is a part of vast electromagnetic spectrum.

Due to the large extent of the electromagnetic spectrum it was divided into several portions (Figure 1.1). Borders of these portions are not precisely specified, they smoothly transition from one to another. Photons from each part of the spectrum exhibit similar properties based on the concept of particle-wave dualism. Photons from the high-frequency end of the spectrum behave mostly like particles while photons from the other end behave mostly like waves.

1.1.1 Radio and microwave radiation

Microwave and radio portions lie on the long-wavelength end of the electromagnetic spectrum. Because of their very similar properties and nearly identical detection technology, we will from now on refer to these parts collectively as radio waves.

Radio waves together with visible light share one advantage over the rest of the spectrum. Thanks to the physical properties of our atmosphere these two parts of the spectrum are (nearly) unimpeded by it so ground-based observations are possible. For radio waves this 'window' spans approximately from 15 MHz to 1 THz. Above the high-frequency end, radiation from space is mostly absorbed by the molecules present in our atmosphere, mainly by H₂O and O₂. This effect can be lowered by observations made from high-altitude and low-humidity environments, which allows us to examine the distribution of these molecules in space. The main blocking element below the low-frequency end is the Earth's ionosphere where free electrons can absorb or scatter the incoming radiation. The only solution to this obstruction are space-based observations.

As mentioned above, radio waves exhibit mostly wave characteristics. This means that diffraction and interference are a prominent phenomena that can be used for our benefit, as will be described in the following paragraphs.

1.2 Apertures synthesis

To make detailed observations of distant objects we need a telescope. Every telescope is physically limited by diffraction that limits angular resolution of the image. The minimal angular resolution σ is defined as

$$\sin \sigma \propto \frac{\lambda}{D}, \quad (1.1)$$

where λ is the wavelength of observed signal and D is diameter of the telescope. In small angle approximation we get a simple relation

$$\sigma \propto \frac{\lambda}{D}. \quad (1.2)$$

The proportional constant k for equality in the previous equation ($\sigma = \frac{k\lambda}{D}$) is dependent on the definition of condition for two point sources to be distinguished from one another. For circular aperture, the value is $k = 1.22$ for definition used in optical observations (radius of Airy disk) and $k = 1.15$ for definition used in radio observations (FWHM of beam pattern central peak).

If we wanted to achieve the same angular resolution as Hubble Space Telescope ($\sigma \approx 0.05$ arcsec) at millimeter wavelengths, we would need a telescope with diameter $D \approx 4$ km! Telescope of this diameter is too large to be built. Largest fully steerable radio telescopes are in Effelsberg, Germany and in Green Bank, USA with diameter of 100 m. Larger telescope dishes were built, but pointing of the telescope is achieved by moving receiver suspended above the dish. This construction allows to observe only areas of the sky around zenith with deviation of the order of ones to lower tens of degree, greatly reducing the possible area of sky that can be observed. Largest telescope of this construction is FAST (Five-hundred-meter Aperture Spherical Telescope), China with effective dish diameter of 300 m.

To get higher angular resolution observations we need to use aperture synthesis. This method changed radio astronomy forever so much that its creator Martin Ryle was awarded half of the 1974 Nobel Prize in Physics. The biggest advantage of using aperture synthesis

is achievable angular resolution. Aperture synthesis is performed with array of many smaller antennas whose signal is then processed to make the final image. Sophisticated processing techniques allow us to reconstruct images with angular resolution of a telescope the size of the whole array.

1.2.1 Basic principles

Observations of the source are carried out by an array of radio telescopes with known positions on the Earth. Each possible pair of antennas is then treated as two-element interferometer. Signals from the antenna pair is then combined and further processed. Output of the processing is the value of 2D visibility function, which is connected to the intensity distribution of the source by Fourier transform. Value of visibility is dependant only on \vec{b}/λ where \vec{b} is the baseline (projected position of one antenna in regards to the second one) and λ wavelength the observation was carried out on.

Each pair of antennas gives us two points in the uv -plane, where u and v are the components of the \vec{b}/λ . By observing the source with many different baselines we obtain more points in the uv -plane. To extend the number of sampled points, we use rotation of the Earth which alters the projected relative position of the antennas during observation, to fill uv -plane with as many samples as possible.

When we collect enough samples, we can make the Fourier transform of the uv -plane to obtain so called 'dirty image' of the sky. This image can be than 'cleaned' and we get the final image of the observed object.

Precise mathematical formulation can be found in literature, e. g. Marr et al. 2021 or Burke et al. 2019.

1.3 Atacama Large Millimeter/submillimeter Array

The Atacama Large Millimeter/submillimeter Array (shortly ALMA) is a radio interferometer made up from 66 telescopes in Chile build by partners from around the world. Chajnantor plateau in the Atacama desert was chosen for two main reasons - its high altitude (around 5000 m) and low-humidity environment. Both of these help with the suppression of negative effects of the atmospheric absorption. The array saw its 'first light' in 2011 with the whole array operational from 2013.

1.3.1 Technical information

The array observes the universe in several bands (Table 1.1) from 84 MHz to 950 GHz, with future low-end boundary at 35 MHz after the installation of band 1 and 2 receivers is finished. To achieve the best results at low-resolution and high-resolution ends it is divided into 2 groups with 3 separate designations during observation.

- **Main array**

The main array is composed of 50 12m dish antennas provided by North American



Figure 1.2: ALMA antennas (ESO/C. Malin (christophmalin.com))

and European partners. These antennas can be moved across variety of separations, with maximum separations ranging from 150 m to 16 km allowing for a range of spatial resolutions of 0.7 arcsec - 6 mas, depending on the chosen configuration and band. This makes it possible to carry out observations with levels of detail even higher than the Hubble Space Telescope can produce at visible wavelengths.

- **Atacama Compact Array (ACA)**

ACA consists of 12 7 m antennas and four 12 m antennas. The 7 m antennas can be moved closer together which makes detection of extended sources in the area of interest possible. The four 12 m antennas are used to observe the total power coming to us from the object of interest. This information is unobtainable from an interferometer due to its operational principle.

Band	Frequency [GHz]	Wavelength [mm]
1	035 - 050	8.57 - 6.00
2	067 - 090	4.48 - 3.33
3	084 - 116	3.57 - 2.59
4	125 - 163	2.40 - 1.84
5	163 - 211	1.84 - 1.42
6	211 - 275	1.42 - 1.09
7	275 - 373	1.09 - 0.80
8	385 - 500	0.78 - 0.42
9	602 - 720	0.50 - 0.42
10	787 - 950	0.38 - 0.32

Table 1.1: Bands of the ALMA receivers. From www.almaobservatory.org, acc. 5/2022

Chapter 2

Ram pressure stripping

One of the major influences on the evolution of galaxies is coming from the surrounding environment. Difference in evolution between dense environments and field galaxies has been established by Dressler 1980. The main difference can be found while exploring the atomic and molecular contents which are on average lower for cluster galaxies.

There are two main mechanisms that can explain this phenomenon. First is of gravitational origin. Galaxies can be perturbed by interactions with other members of the group/cluster or by the the potential well of the rich region itself. These two effects can be combined by multiple fly-bys, usually called galaxy-harassment.

Second mechanism is based on hydrodynamics. This mechanism is most prominent for galaxies with high velocity moving through hot and dense ICM. This can lead to evaporation of the ISM (e.g. Cowie et al. 1977) or to removal of the gas by the generated outer dynamical pressure (ram pressure stripping, e.g. Gunn et al. 1972). At the interface between the cold ISM and hot ICM, creation of instabilities leads to removal of the gas from the galactic disc.

There is an easy way to distinguish between these two families of mechanisms - while the gravitational interactions act on the galaxy as a whole (i.e. all of its components similarly, including the stellar disc), hydrodynamic processes are acting only on the ISM (atomic and molecular gas). Other smaller scale processes can also alter the galactic morphology but they are negligible in comparison with the main mechanisms.

RPS is not only limited to stripping ISM from members of galaxy clusters, it is present everywhere when there is non-negligible motion between an object and its surrounding environment. These can be mergers of galaxy clusters, bending of jets or even individual stars with strong stellar winds.

2.1 Physical process

X-ray emission of the ICM that is trapped in the potential well of the cluster indicates that the ICM has high temperature, typically $T \approx 10^7 - 10^8$ K and density $n_{\text{ICM}} \approx 10^{-3} \text{ cm}^{-3}$ (Dressler 1980). When galaxy moves through this environment, it experiences a drag force by the ICM that creates pressure expressible as

$$P = \rho_{\text{ICM}} v^2, \quad (2.1)$$

where ρ_{ICM} is the local density of the ICM and v is the relative speed of the galaxy and ICM (Boselli et al. 2021).

This pressure is then able to remove gas from the galaxy if it overcomes the gravitational forces of the host galaxy. As can be seen in Equation 2.1, RPS is dependant on the properties of the ICM as well as the properties of the galaxy moving through it. The hydrodynamic essence of the RPS process is based on the interaction between two gas phases (hot ICM vs cold ISM). Stars are not affected by this interaction because of their small interaction cross-section.

2.2 Observable impact on galaxy



Figure 2.1: Example of a jellyfish galaxy with tail created by RPS, galaxy D100 in Coma cluster, credit: [ESA/Hubble & NASA, Cramer et al.](#)

The most prominent feature of objects undergoing RPS are one-sided "cometary" tails created from stripped ISM. These tails are observable at many different wavelengths, dependant on the phase of the present gas (atomic, molecular, ionised). Galaxies with asymmetric extraplanar features are sometimes called "jellyfish" galaxies (introduced by Chung et al. 2009). Definition of "jellyfish" galaxies was revisited by Ebeling et al. 2014. To be considered "jellyfish" galaxy it has to exhibit the following features:

1. a strongly disturbed morphology indicative of unilateral external forces
2. a pronounced brightness and color gradient suggesting extensive triggered star formation
3. a compelling evidence of a debris trail

4. the directions of motion implied by each of these three criteria have to be consistent with each other

Galaxy with morphology satisfying all the above criteria may not be strictly a result of RPS event. To consider jellyfish galaxy a product of RPS event, all stars in the tail (if any) must have formed in situ after the stripping process took place.

In RPS interaction all the gas is being stripped from the outer regions of the galaxy inwards, leaving behind truncated gas disc when compared to field counterparts. The remaining gas component of the galaxy disc can also be characterised by asymmetric distribution. RPS event is also expected to alter the kinematics of the gas component by dislocating its kinematic centre with respect to the stellar disc and even altering the velocity field in the border regions.

2.3 Impact on galaxy evolution

Removal of the gas reservoirs in the outer regions of galaxy has tremendous effect on the future of the galaxy. Absence of the diffuse atomic gas results in decrease of star formation mostly in outer regions. For dwarf systems with shallow potential well, RPS is expected to possibly have devastating effects and stop star formation all-together.

When it comes to the stripped gas, its fate is not yet precisely known. Simulations and observations present two scenarios. Either the gas can fall back onto the galaxy once it gets to the outskirts of the cluster where RPS is negligible (Vollmer et al. 2001) or it can create long cometary tails. The stripped gas is mixing with the surrounding ICM (Zabel et al. 2019) and depending if heating or cooling processes dominate, may host star forming regions (e.g. Ming Sun et al. 2021). Rogue stars created in these regions than contribute to the so called intra-cluster light (e.g. Montes 2019)

For further information on the subject of RPS, we recommend referring to Boselli et al. 2021.

Chapter 3

The galaxy ESO137-001

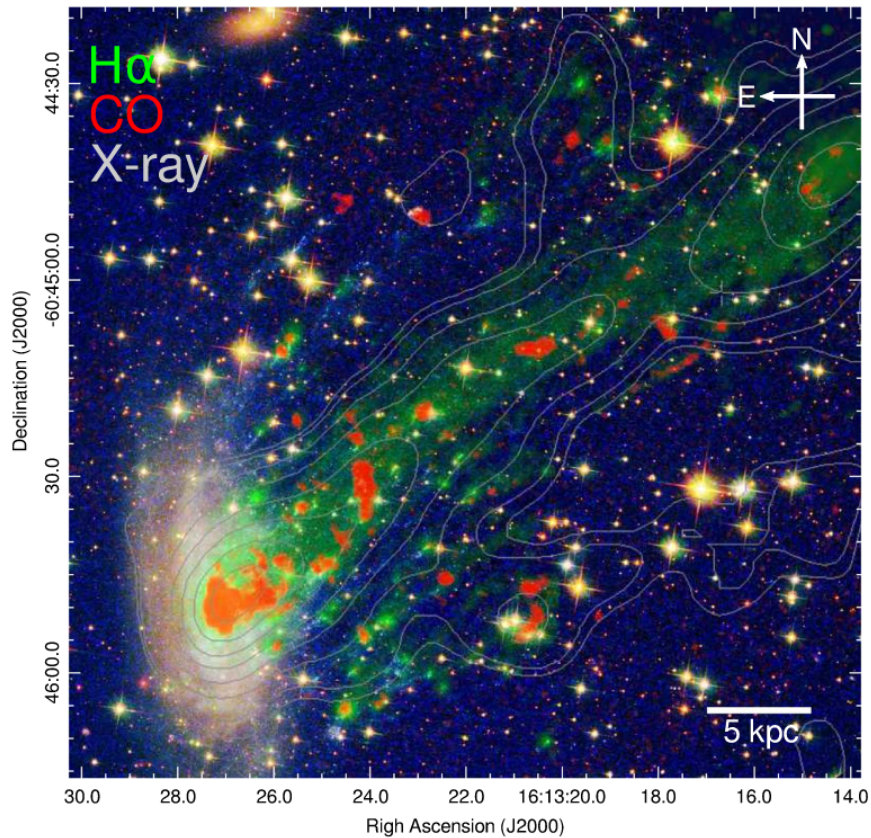


Figure 3.1: Combination of four observations of ESO137-001 from different instruments. Background is from HST WFPC3 observations in visible bands. They are overlaid with green areas of MUSE $H\alpha$ data, *Chandra* X-ray data in contours and ALMA CO(2-1) emission in red. Taken from Jáchym, Kenney, et al. [2019](#)

ESO137-001 is a barred spiral galaxy located in the southern sky Norma cluster (Abell 3627). General information about the galaxy is in [Table 3.1](#). [Figure 3.1](#) shows gas-stripped (red) galaxy with most of the molecular gas concentrated in the inner-most regions.

The Norma cluster can be compared in number of members to clusters like Coma or

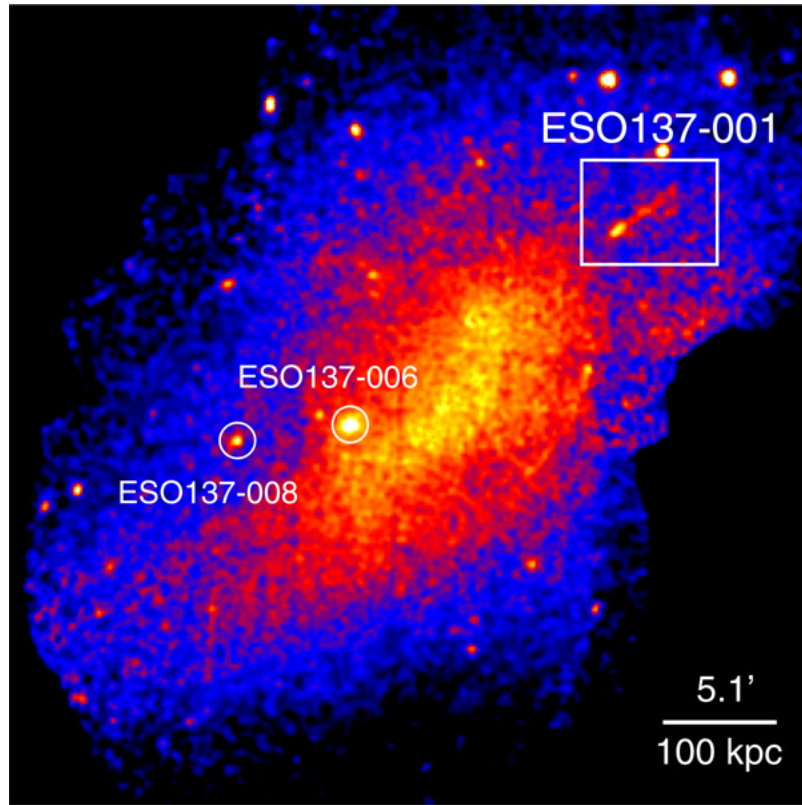


Figure 3.2: Central parts of the Norma cluster. X-ray image from *XMM Newton* in energy range 0.5-2 keV. Rectangle shows the position of ESO137-001. Taken from Jáchym, Combes, et al. 2014

Perseus. The whole cluster appears strongly elongated with the center laying near the position of the cD galaxy ESO137-006 (refer [Figure 3.2](#)). Spiral and irregular galaxy members appear to be highly affected by interactions in the cluster. In the right upper corner we can see our galaxy of interest - ESO137-001. ESO137-001 is being projected at about 280 kpc in the NW direction from the cluster center. Radial component of the orbital velocity is $\approx -195 \text{ km s}^{-1}$ (Jáchym, Combes, et al. 2014). They also estimated that the spatial velocity of the galaxy in the cluster is $> 3000 \text{ km s}^{-1}$, placing the orbital motion mostly in the plane of the sky.

Observations of the galaxy from *Chandra* and *Newton* revealed long, narrow, 70 kpc long X-ray tail (M. Sun, Jones, et al. 2006). Further optical observations revealed 40 kpc long $\text{H}\alpha$ tail (M. Sun, Donahue, and Voit 2007) corresponding with possible star formation outside of the galactic disc (over 30 detected HII star-forming regions in the tail). Radio observations also showed presence of cold CO tail (Jáchym, Combes, et al. 2014), the first evidence of molecular phase in the tail of jellyfish galaxy. The presence of this gas tail and unperturbed stellar disc (see [Figure 3.1](#)) clearly indicate ram pressure stripping interaction.

ESO137-001 is a jellyfish galaxy with the best multi-wavelength coverage (from X-ray to radio emission) of the stripped tail. While most works are focused on the RPS tail, the kinematic properties of the disc region remain largely unexplored. In this thesis we will analyse and describe kinematics of the gaseous component of the galactic disc using

observations carried out by ALMA in 2015.

Parameter	Value
Type	SBC
RA ^a (J2000, ICRS)	243.3638°
Dec ^a (J2000, ICRS)	-60.7641°
Angular size ^a	(0.357 x 0.193) arcmin
position angle ^e	(8.8 ± 1.6)°
inclination ^d	61 - 67 °
$v_{\text{rad, optical}}^{\text{b}}$	(4630 ± 58) km s ⁻¹
$v_{\text{rad, radio}}^{\text{c}}$	4577 km s ⁻¹
Luminosity distance ^f D_L	69.6 Mpc

^a From 2MASS (Skrutskie et al. 2006)

^b From SAAO survey (Woudt et al. 1999)

^c From Jáchym, Combes, et al. 2014

^d From M. Sun, Donahue, and Voit 2007

^e From Luo et al. in prep., 2022

^f From M. Sun, Donahue, Roediger, et al. 2010

Table 3.1: Basic information about ESO137-001

Chapter 4

Data processing

4.1 Software

For data analysis presented in this work we used a variety of software and scripts.

Data viewing and rendering was done using CARTA (<https://cartavis.org/>). Creation of integrated flux map (moment 0, see [section 4.4](#)) and Position-velocity diagrams (see [section 4.6](#)) was done in beta version CARTA3.0.0-beta.2b which is the first version with integrated PVD creation. This software is still in development with great potential in the future.

For generating moment 1 and 2 maps ([section 4.4](#)) we used CASA (*Common Astronomy Software Application*, <https://casa.nrao.edu/>) which is the recommended main processing software for data obtained by ALMA. It contains methods for processing of single-dish and aperture synthesis data with automated pipelines for ALMA and VLA arrays. The particular version of this software we used was CASA 6.3.0.48.

For Disc modelling ([section 4.7](#)) we used 3D BBarolo code (Di Teodoro et al. 2015), specifically its 2DFIT task. It is a ring fitting model developed especially for analysis of disk-like object kinematics from emission-line observations.

For special tasks, self-written Python scripts were used. Definitions of the used functions are in [Appendix](#). Specific functions are mentioned at relevant points in the text.

4.2 Used data

For our analysis we used two sets of data

1. The main data set is ALMA CO(2-1) observation - project code 2015.1.01520.S. The downloaded data-cube from ALMA archive is result of Additional Representative Images for Legacy (ARI-L) project (Massardi et al. 2021). The data collection was carried out with the 12 meter antennas of the main array of ALMA in compact configuration (baselines 15.1-469 m). There is also a data-set obtained by the 7 meter antennas from the same project, but it is not relevant for our kinematics analysis due to the low resolution.

To cover the whole area of the galaxy and its tail, the final image is a mosaic of

130 pointings. The angular resolution, given by the synthesized beam, is around 1.3×1.1 arcsec and the spectral resolution is around $488 \text{ kHz} \approx 0.64 \text{ km s}^{-1}$.

The observed CO(2-1) line is one of the rotational lines of the CO molecule with rest frequency 230.538 GHz (in ALMA band 6). It is mainly used as a tracer of molecular gas.

2. Complementary set of data are from MUSE (Multi Unit Spectroscopic Explorer) instrument at VLT of the European southern observatory. MUSE is an integral spectrograph operating at visible wavelengths.

ESO137-001 data were obtained in in the Wide-field mode covering area of $1 \times 1 \text{ arcmin}^2$.

The moment 1 map created from these data was graciously provided by Ming Sun (Alabama University in Huntsville, USA)

The pixel scale of both data-sets is $1 \text{ px} = 0.21 \text{ arcsec} \approx 70 \text{ pc}$ at the distance of the galaxy (Table 3.1).

4.3 Data preparation

In our analysis we focused purely on the disc of ESO137-001. To reduce the size of the ALMA data that go through each processing step, we used only a part of the whole data cube. In spectral axis we narrowed the frequency range to only the values for which we can see emission from the gas disc ($226.9679 \text{ GHz} - 227.0656 \text{ GHz}$). In spatial coordinates we cut out only small area around the disc (Figure 4.1). The data-cube cropping was done in CARTA. This left us with data file with size of only 6.3 MB from the original size of 19.8 GB . File of this size is much easier to handle and analyse.

For PVD creation (section 4.6) and fitting of the stellar disc (section 4.7) MUSE moment 1 map had to be altered by removing masked-out foreground stars. This was done using Python script that changed all values of radial velocity exceeding $|v_r| = 100 \text{ km s}^{-1}$ to `numpy.nan` ('not a number'). Difference between moment map before and after can be seen in Figure 4.2.

4.4 Moment maps

While working with data in form of spectral cube, the hardest part is its visualization. We are working with two spatial coordinates, spectral coordinate and usually flux density. To make some properties easier to see it is advantageous to either slice the data by specific plane (channel maps, PVDs in section 4.6) or collapse usually the spectral axis into a single value by linear combination of individual channels. This results into a 2D object generally called moment map. General expression of this process is

$$M_m(x_i, y_i) = \sum_k w_m(x_i, y_i, v_k) * I(x_i, y_i, v_k) , \quad (4.1)$$

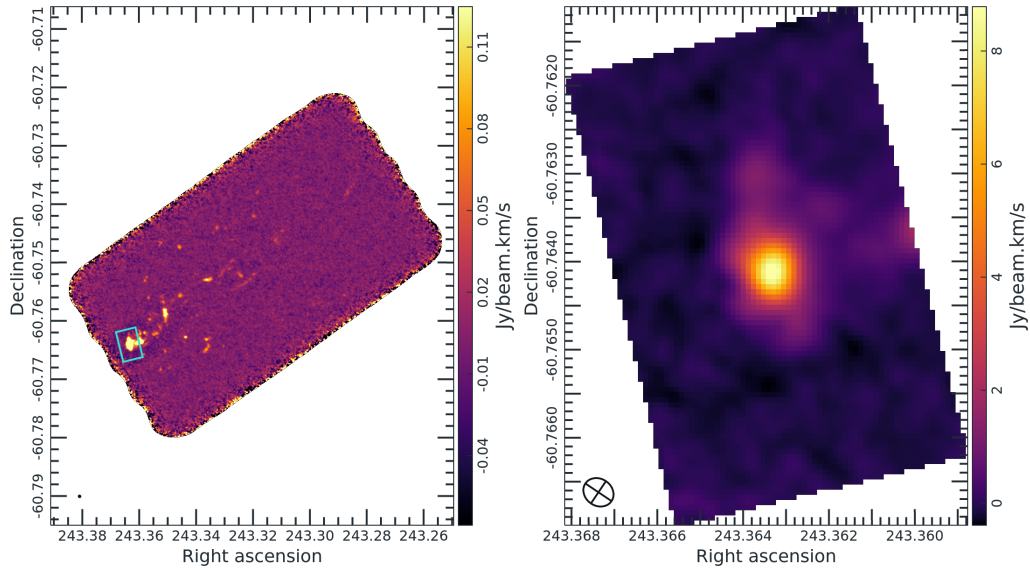


Figure 4.1: ALMA view of the molecular gas distribution in the ESO137-001 galaxy and its tail. left: Integrated flux map (mom. 0) of the whole mosaic, right: Integrated flux map of used cropped data set; Ellipse in the lower left corner shows the size of the beam.

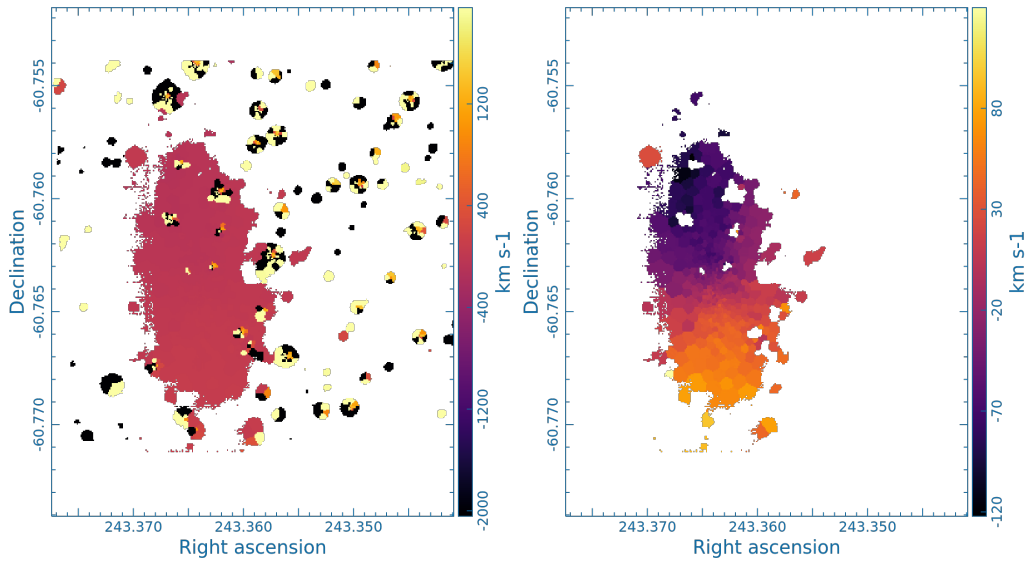


Figure 4.2: Velocity field (moment 1) of the ESO137-001 stellar disc from MUSE before and after star removal

where index m represents the type of moment map, i specifies pixel, k channel and w_m is moment-specific weight for each value of I . x and y are spatial coordinates and v spectral coordinate.

By altering the w_m coefficients we get maps showing different properties of the data. Different 'moments' are usually referenced by universal whole number index from -1 to 11. Each moment shows different property of the data. In this work we will describe only moments 0, 1 and 2 (Figure 4.3). To generate these moments, we used CARTA (Spectral

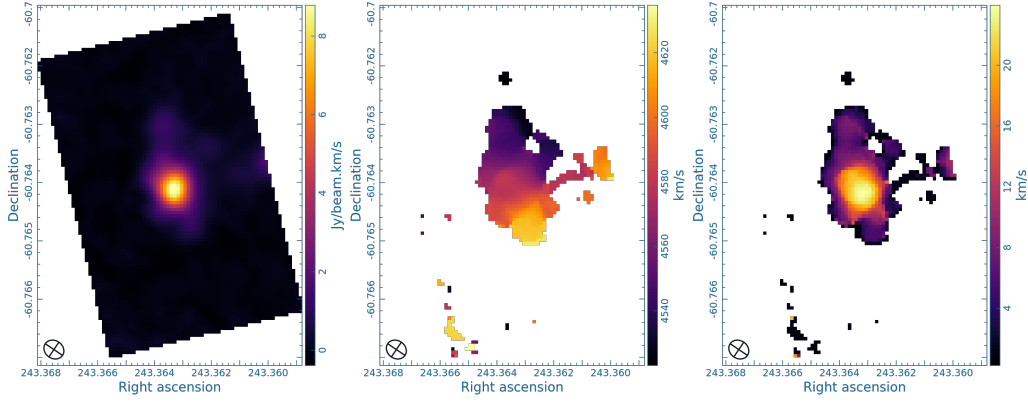


Figure 4.3: Moment maps of the molecular gas disc of ESO137-001; from left to right: moment 0, moment 1 and moment 2

Profiler/Moments) and CASA (immoments). To get rid of values for noise in moment 1 and 2 maps, we also set the minimal flux density for included pixels to $0.02 \text{ Jy beam}^{-1}$. This left us with maps that show mostly values for the disc emission.

Mathematical expressions for moments we used are

$$M_0 = \Delta v \sum I_i, \quad (4.2)$$

$$M_1 = \sum \frac{I_i v_i}{M_0}, \quad (4.3)$$

$$M_2 = \sqrt{\sum \frac{I_i (v_i - M_1)^2}{M_0}}, \quad (4.4)$$

where Δv is the spectral resolution.

Moment 0 map (Figure 4.3, left panel) shows integrated intensity along the whole available spectral range. This is useful for finding areas from where most of the emission comes from. In the case of ESO137-001, it shows highly asymmetric distribution of gas. The northern region is far more extended than the southern one, which is most likely a result of the geometry of the RPS interaction with the disc. The emission is also extended in the western direction where it connects to the innermost parts of the tail.

Moment 1 map (Figure 4.3, middle panel), usually called velocity field, shows mean radial velocity of the observed emission. It also shows that the molecular disc is dominated by rotation, reaching rotational velocity of approx. 40 km s^{-1} relative to the systematic velocity of the galaxy.

Final moment 2 map (Figure 4.3, right panel) is showing the dispersion of radial velocities. It peaks in the central part with value of approx. 25 km s^{-1} . It drops down with increasing radii, approaching zero at the edge of the disc.

Comparing moment 1 maps of stellar and gas disc (Figure 4.4) clearly shows that CO emission, used to trace molecular gas, is constrained the central parts of the galaxy. The radius of the gas disc is about $4\text{-}5 \text{ arcsec} \approx 1.3\text{-}1.6 \text{ kpc}$. Beyond this radius most of the ISM is depleted and now contributes to the tail. The CO flux from the disc area corresponds to H_2 mass of around $7 \cdot 10^8 M_\odot$, typical for the central regions of gas-rich galaxies (Jáchym,

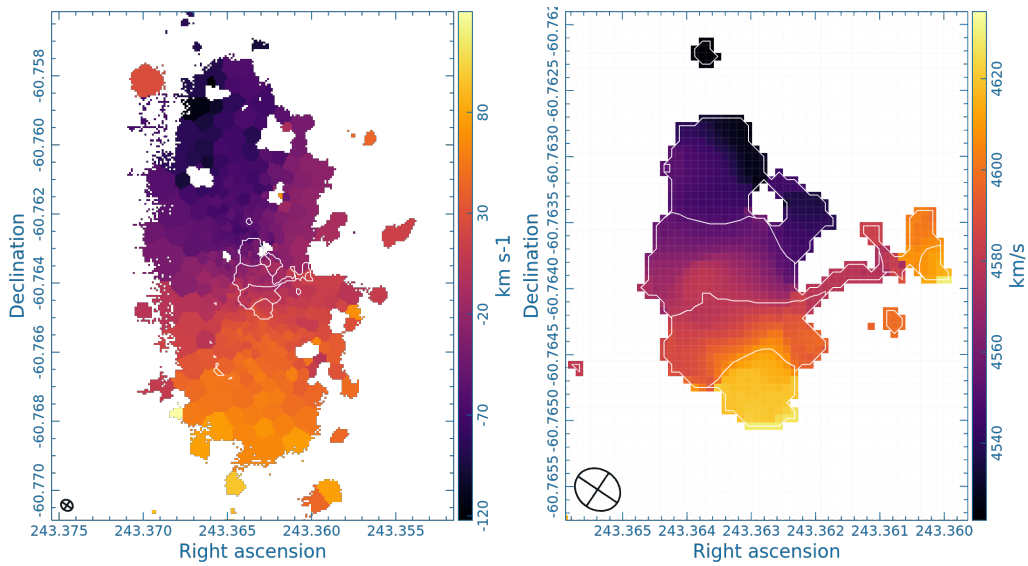


Figure 4.4: Extent of the CO emission (right) compared to the MUSE data for the stellar disc (left) with CO contour overlay.

Kenney, et al. 2019). This mass should be enough to retain the remaining gas in the disc and protect it from effects of further stripping.

Meaning of other moment indexes can be for example found in the CASA manual for immoments method (manual, acc. 5/2022).

4.5 Disc center

Next important task before we could continue our analysis was determination of the reference disc center. This can be achieved in many ways and the final position is dependant on the method.

For our analysis of PVDs, the best reference point would be the kinematic center of the disc. Unfortunately this was not an option for us due to the highly perturbed distribution of the molecular gas.

In our case we determined reference central point by fitting 2D Gaussian peak to the moment 0 ALMA CO(2-1) map. This method assumes that the emission peak lies in the center of the galaxy.

The resulting image coordinates are

$$x = 39.69 \text{ px} \quad (4.5)$$

$$y = 49.32 \text{ px} \quad (4.6)$$

After transformation of image coordinates to WCS we get

$$\text{RA} = 243.3633^\circ \quad (4.7)$$

$$\text{dec} = -60.7641^\circ \quad (4.8)$$

Considering the results of follow-up analysis (mainly [section 4.6](#)), these coordinates represent adequate reference point for the molecular disc center. Comparing these values with those presented in [Table 3.1](#), an offset of ≈ 0.87 arcsec in the western direction is evident. This can be possibly result of RPS pushing the molecular disc in the direction consistent with the geometry of the interaction. This possibility is further discussed in [subsection 4.6.4](#).

4.6 Position-velocity diagrams

Position-velocity diagram (PVD) is a diagram presenting radial velocity distribution along a specified direction with given width. In the case of a data cube, the diagram shows spectral distribution of the observed flux along specified spatial direction. Creation of PVD from moment 1 map results in a graph of mean radial velocity as a function of the linear offset.

4.6.1 Linear regions

To study the kinematics in different parts of the disc we created linear regions along major and minor axes and sets of lines parallel with them, indexed by the position relative to the central line ([Figure 4.5](#)). Position angle of the stellar disc is $\approx 8.8^\circ$ ([Table 3.1](#)).

To hold the parallel nature of the lines, respective regions were generated as CASA region file using self-written Python script ([appendix B](#)). Spacing of the lines is equal to $d_{\text{major}} \approx 1.2$ arcsec ≈ 400 pc for major axis and $d_{\text{minor}} \approx 2.5$ arcsec ≈ 830 pc for minor axis.

The linear offset along the PVD direction is defined: In the case of lines parallel with the major axis, 0 offset corresponds to position on the minor axis and vice versa. For major axis lines, offset rises from bottom to top (south to north) and for minor axis from left to right (east to west). With defined lines we can proceed to study different properties of the PVDs along them.

4.6.2 PVDs along principal axes

First we generated PVDs along the major and minor axes ([Figure 4.6](#)). We used averaging width of $3 \text{ px} \approx 210 \text{ pc}$.

PVD along the major axis has a shape characteristic for spiral galaxies, as is our own, but perturbed by the affects of the ram pressure (more below). There are two components visible - one nearly vertical, reaching up to $\pm 50 \text{ km s}^{-1}$ relative to the systematic velocity, and second slowly rising up to the radius of around 3 arcsec reaching constant velocity of around $\pm 40 \text{ km s}^{-1}$ relative to the systematic velocity. These two components are not resolved in the minor axis PVD, most likely due to the low spatial resolution of the data. The steep central component is most likely evidence of barred structure in the central parts

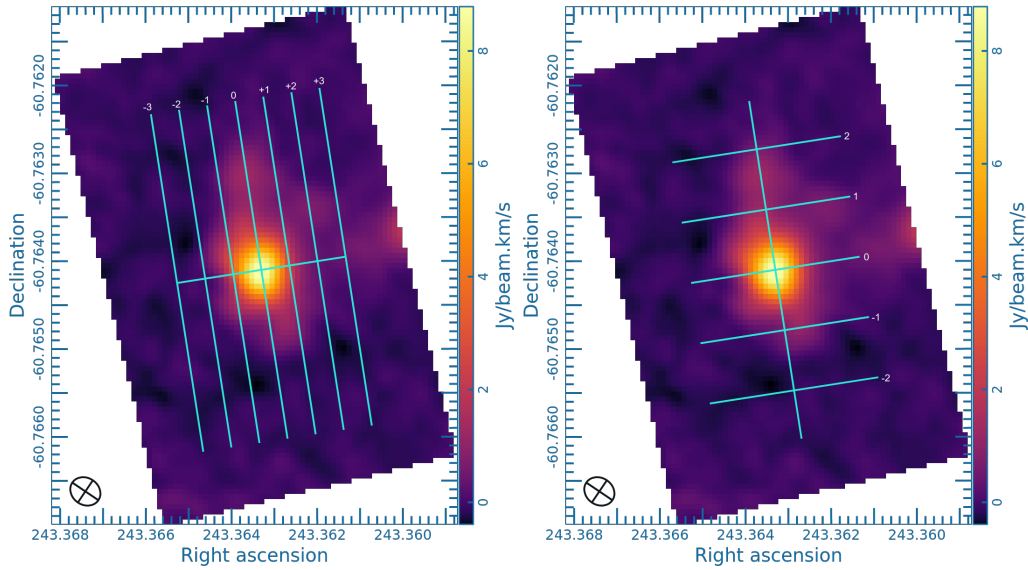


Figure 4.5: Used PVD lines marked on moment 0 map with indexes. Perpendicular line marks 0 offset. left: major axis PVDs, right: minor axis PVDs

of the galaxy (e.g. Athanassoula et al. 1999). The latter slow-rising component, so called 'S-curve', is typical for all spiral galaxies.

Due to the effects of RPS, the major and minor axes PVDs show a number of asymmetries. The most prominent one in the major axis PVD is the asymmetric clipping of the 'wings' at small radii due to the geometry of the RPS interaction (discussed in section 4.4). Another striking asymmetry is located in the middle of the diagram. We can clearly see that the peak intensity is dislocated from the center of the S-curve. While similar dislocations can be observed even in unperturbed galaxies, in our case it can be enhanced by the RPS in ESO137-001.

Minor axis PVD shows asymmetrical distribution of emission which is usually reminiscent of circle or diamond. Again, this is most likely result of the interaction geometry. RPS is acting from the left (east), compressing the leading side and prolonging the trailing side. This is also consistent with the presence of tail in that direction.

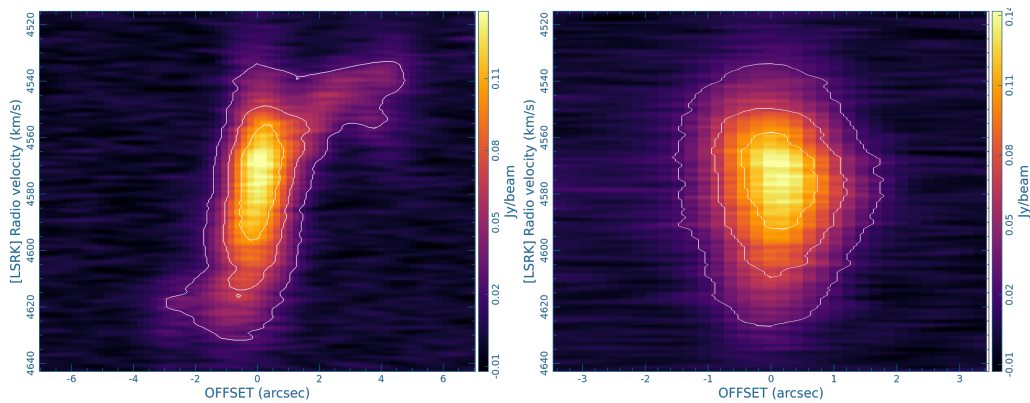


Figure 4.6: PVDs along the major (left) and the minor (right) axes

We also explored the effects of the used averaging width. We created PVDs with wider averaging areas: 6 and 10 px which corresponds to scales of 426 and 710 pc respectively (Figure 16 in Appendix). Strength of the effect is not significant. With increasing width the amount of details decreased together with the over-all intensity. This is due to inclusion of larger scale structures of the galaxy, lowering the contribution of local deviations.

Comparison to the unperturbed galaxy NGC1386

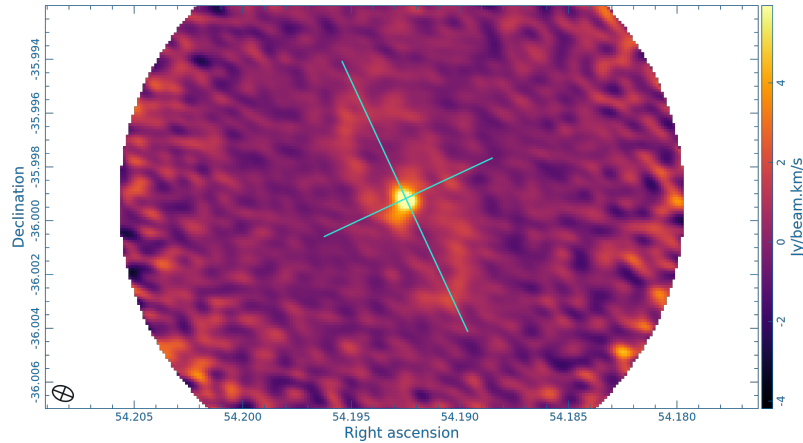


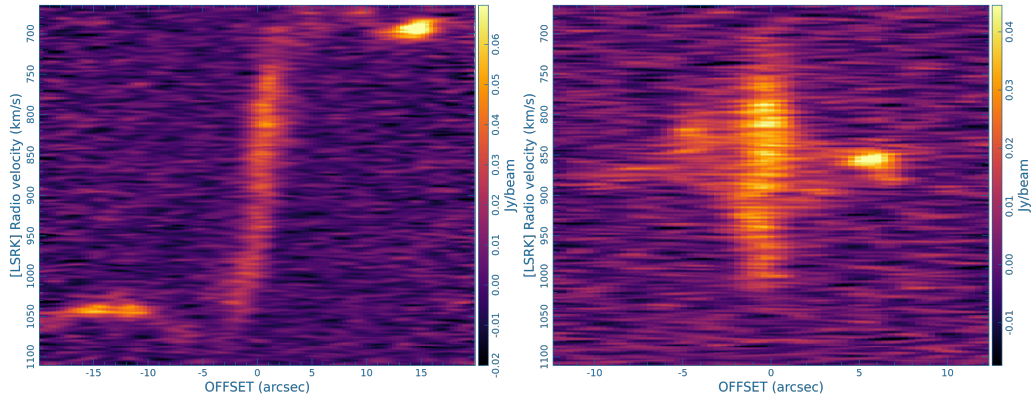
Figure 4.7: NGC1386 moment 0 map with used PVD lines; long=major, short=minor

To better demonstrate the effect of RPS we compare our PVDs with ones from unperturbed galaxy. We chose galaxy NGC1386, member of the southern sky Fornax cluster. Member galaxies of this cluster were observed by ALMA (Zabel et al. 2019). This galaxy is not spared from interaction with the cluster, however no noticeable effects are observed, making it suitable for our comparison. NGC1386 is a spiral galaxy and as shown in Zabel et al. 2019, its PVD shows features similar to PVDs described above, mainly the x-shaped morphology connected to the presence of a bar.

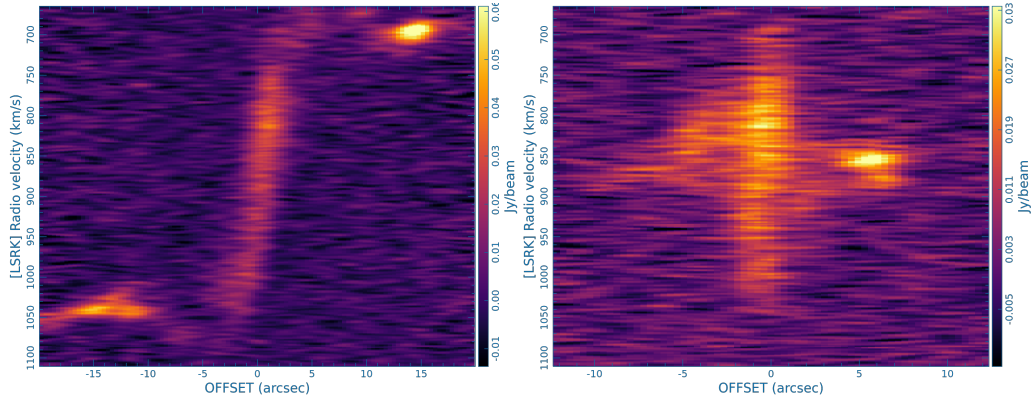
We downloaded the data from ALMA Archive (SPW3 from project 2015.1.00497.S) and generated PVDs along the major and the minor axes (Figure 4.7). We used 2 averaging widths - 3 and 10 px. Resulting PVDs can be seen in Figure 4.8.

The comparison shows that the PVDs of an unperturbed galaxy are quite symmetrical with S-curve along the major axis and a diamond shape along the minor axis. There is also the nearly vertical component alongside the S-curve, which can be connected with the presence of a bar structure. This barred structure in the central region easily visible in Figure 4.7 close to the minor axis. The vertical feature reaches higher radial velocity compared to the outer plateau parts of the disc. Moving from the center, this results in steep increase in radial velocity which then dips down at the edge of the central structure and connects to the outer plateau region. Similar structure can be seen in our PVDs at the low-velocity end.

In the minor axis PVDs, one can see diamond structure with two pronounced axis. The horizontal one is the result of the rotating disc while the vertical one can be again attributed to barred or disc-like structure in the central regions of the galaxy.



(a) averaging width 3px



(b) averaging width 10px

Figure 4.8: NGC1386 PVDs along major (left) and minor (right) axes

4.6.3 Offset PVDs

So far the analysis was connected only to the principal axes, but to see the true effect of RPS we continued with creation of PVDs along lines parallel to the central principal lines. This allows us to more deeply explore the asymmetries of the molecular gas distribution. The resulting plots can be seen in [Figure 4.9](#) and [Figure 4.10](#). Each row of two diagrams shows PVDs with the same distance from central line. All figures share averaging width of $3\text{ px} \approx 210\text{ pc}$.

While moving away from the central major principal axis in eastern and western direction, PV diagrams exhibit flattening of the slope of the S-curve, expected behaviour of inclined rotating disc. The two columns also clearly show the significant asymmetry caused by the ram pressure stripping. In case of ± 1 diagrams ([Figure 4.9a](#)) we can see that while the western side (right) still shows large spatial and spectral extent of the emission, the eastern side (left) shows suppressed emission outside central regions. This is consistent with RPS pushing the molecular gas in the western direction - the direction of the tail. ± 2 diagrams ([Figure 4.9b](#)) show further decrease of emission extent in the eastern side of the disc. In the extreme case of the ± 3 diagrams ([Figure 4.9c](#)), eastern side has no emission at all while western side retains significant amount of emission coming from the 'bridge' between the disc and the tail.

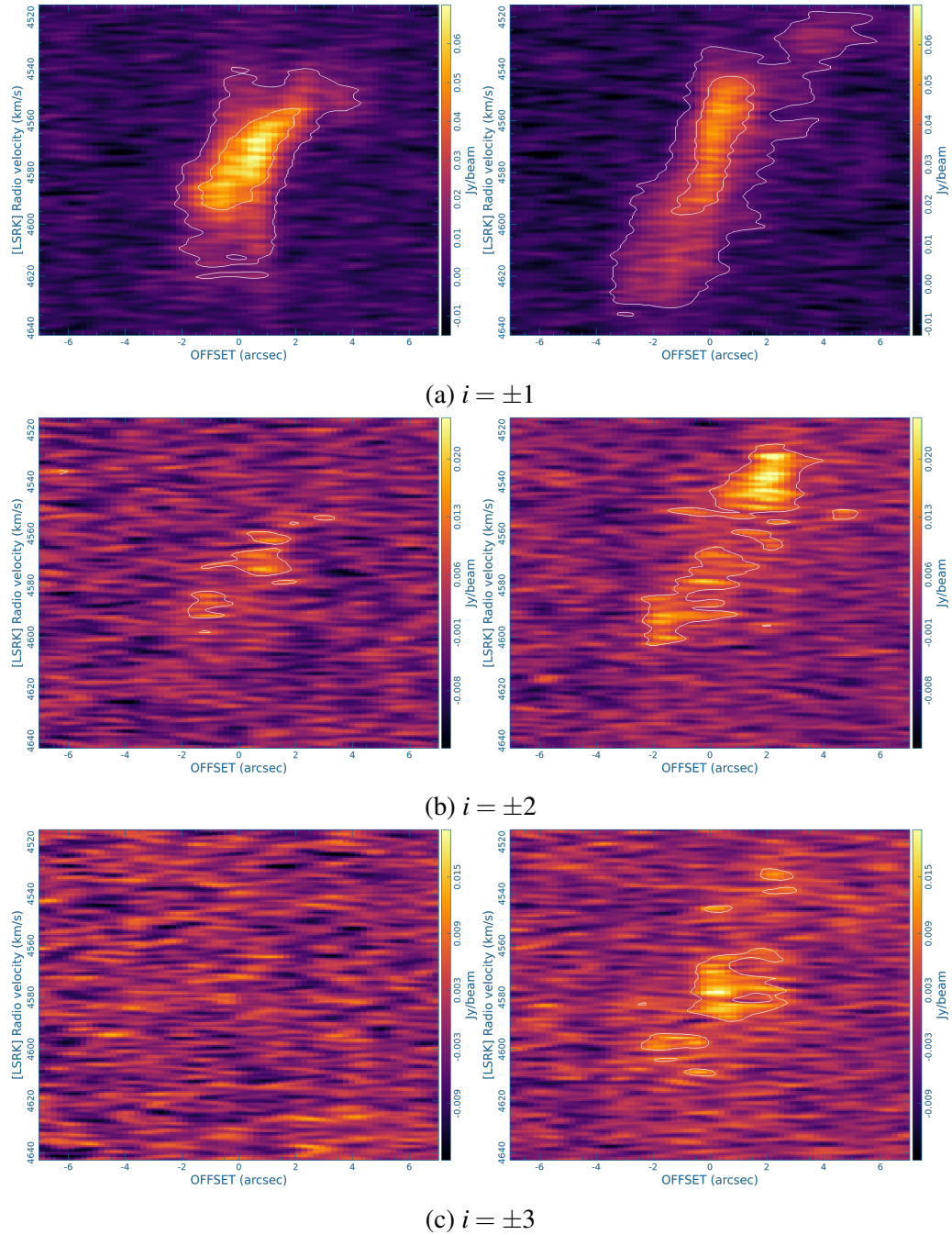


Figure 4.9: PVD symmetries along major axis. Negative indexes (eastern side) are in the left column, positive (western side) in the right.

For minor axis (Figure 4.10) we can again see highly asymmetric distribution. The southern side (right) of the disc is lacking any visible emission in the -2 diagram, while northern side (left) has plenty. Northern end also exhibits sloped profile of emission, possibly coming from a gas cloud being accelerated by ram pressure from the outer regions of the disc into the tail.

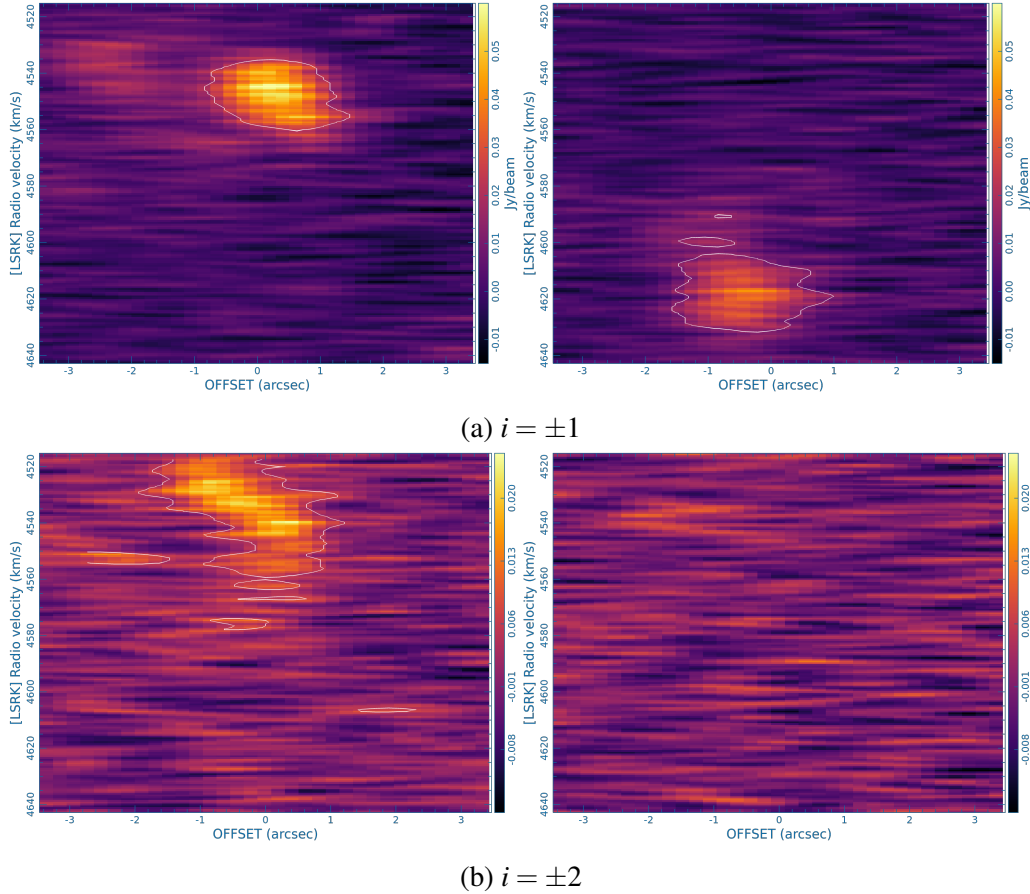


Figure 4.10: PVD symmetries along minor axis. Positive indexes (northern part) are in the left column, negative (southern part) in the right column.

4.6.4 Comparison with stellar disc

To further explore the effect of the ram pressure on the molecular disc we compared the PVD of the molecular gas disc with PVD of the unperturbed stellar disc (see section 2.1)

To compare PVD profiles we first had to transform the absolute radial velocities of the ALMA data into radial velocities relative to the systematic radial velocity of the galaxy. To determine the systematic velocity of the galaxy, we used the symmetry of the PVD (Figure 4.6). In the case of rotating disc, major axis PVD is symmetric and the systematic velocity (velocity of the kinematic center) is exactly in the middle between the velocities of the plateau regions. Using this assumption we derived systematic velocity of the molecular disc of $v_{\text{sys}} \approx 4582 \text{ km s}^{-1}$. This value is close to the velocity derived from single-dish spectral observations by Jáchym, Combes, et al. 2014 (Table 3.1).

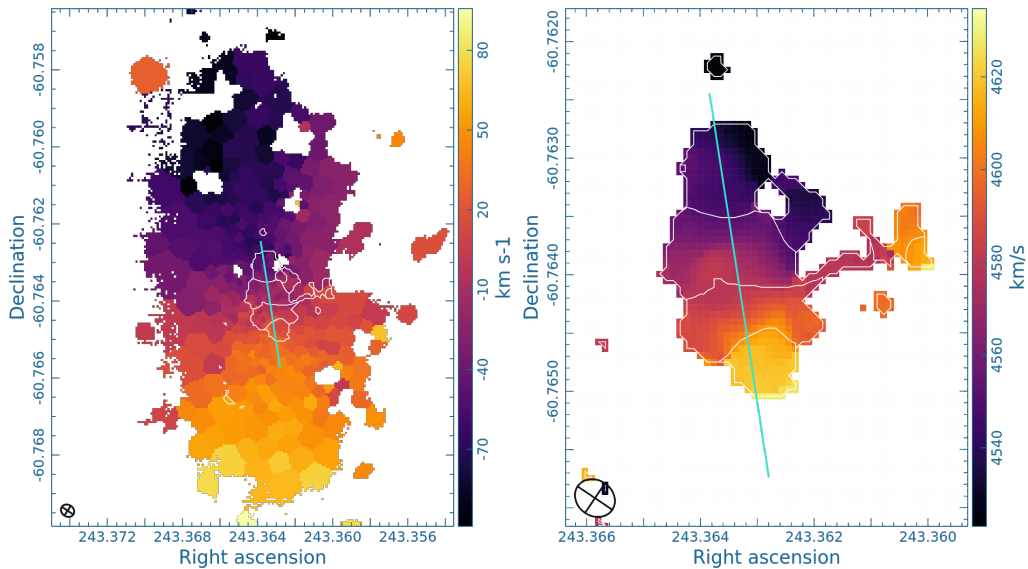


Figure 4.11: Moment 1 map from MUSE (left) and ALMA (right) data. The line segment marks region used for PVD and contours are showing projection of ALMA data on the MUSE set.

We produced the PVDs from moment 1 maps from the VLT/MUSE and ALMA data using self-written script (Appendix C). Used line can be seen in Figure 4.11. We note again that the extent of the molecular disc is radically smaller than the stellar disc. Thus our comparison is done with only the inner-most parts of the stellar disc. The center of the used line has the same WCS coordinates for both maps, those of the CO emission peak (section 4.5 Equation 4.7 and Equation 4.8) and the position angle of the line is 8.8° (Table 3.1). Resulting plot can be seen in Figure 4.12.

The resulting plot shows mostly overlapping curves, suggesting similar rotational profile for both structures. There is large offset present in the red-shifted southern region. This offset is consistent with stronger effect of RPS in this region given by the geometry of the interaction between galaxy and ICM. In the blue-shifted region the two curves match quite well.

In the center of the diagram (zero offset) there is a small systematic offset between the reference point and the PVDs. This may suggest that our reference point does not represent well the kinematic center of neither disc. The offset between the PVDs themselves can imply systematic shift between the two discs. The origin of this offset can be based in RPS. Motion of the galaxy ESO137-001 takes place mostly in the plane of the sky (see chapter 3), there is only small radial component of the orbital velocity ($\approx -195 \text{ km s}^{-1}$) resulting in slight blue-shift of the galaxy relative to the cluster. The RPS tail produced by the geometry of the interaction is then expected to be slightly red-shifted from our point of view. The slight central offset in Figure 4.12 could be consistent with the molecular disc being pushed towards the positive values of offset and higher radial velocities. Even though theory allows such event (see section 2.1), this cannot be decided without more detailed analysis in the future.

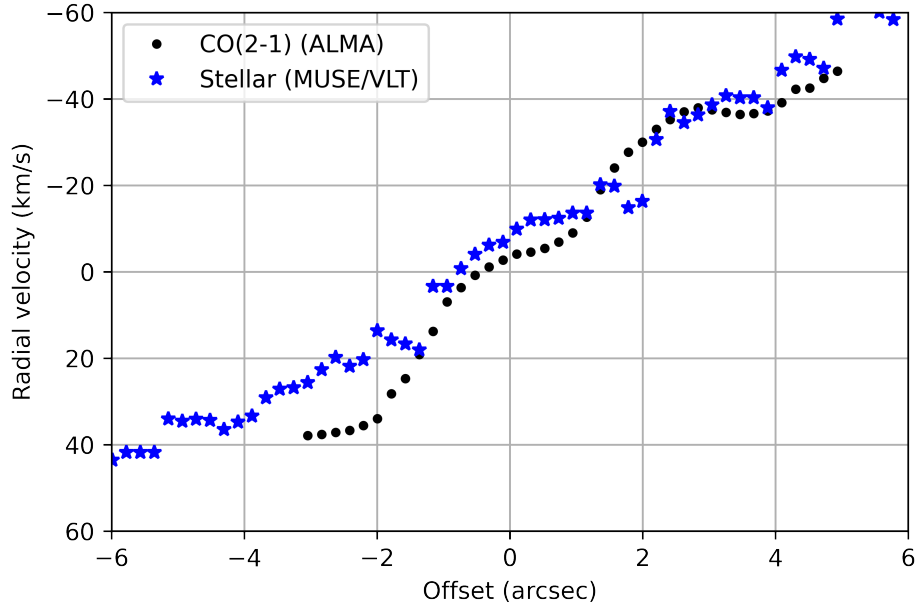


Figure 4.12: Comparison of the ALMA molecular disc and the MUSE/VLT stellar disc PVD along major axis. Radial velocities are relative to the systematic velocity of the galaxy.

4.7 Fitting rotating stellar disc

The goal of the final task is to remove the rotational component from the ALMA CO data to show the motion of the molecular component caused by the RPS. For this we need to create a model of the rotating stellar disc from the MUSE data, which represents the kinematics of the galaxy components unaffected by the RPS. For this task we used 2DFIT method from 3D-Barolo code (Di Teodoro et al. 2015). The 2DFIT routine performs 2D tilted-ring modelling when modelled velocity field is fitted to the observed velocity field.

We used the adapted MUSE data (see section 4.3). We ran the fitting code from command line, using a parameter file to specify input values for the code. Input parameters of the fit can be seen in Table 4.1. The initial XPOS and YPOS correspond to the center coordinates of CO emission (see section 4.5) and the initial PA with INC are from Table 3.1. Remaining parameters were guessed by reviewing input data.

By running the script, we were able to obtain a single rotating disc model for the MUSE moment 1 map (Figure 4.13). The output values of the fit can be seen in Table 4.2. It can be noted that unlike the real data, the fitted model achieves high rotational velocity close to the center. This is most likely a result of the input value NRADII=2, that creates only one ring. The rotation curve would be better represented by use of many rings. Several trials with larger counts of the rings were unfortunately unsuccessful. Instead of smooth rotating galaxy model, the result consisted mostly of many rings with high variation in their parameters (VSYS, VROT, PA, INCL, X&Y CENTER).

We note that the obtained kinematic center coordinates of the stellar disc $RA = 243.3641^\circ$ and $dec = -60.7642^\circ$ are close (offset of ≈ 0.5 arcsec) to those shown in Table 3.1, sup-

porting the credibility of the fitting process. Possibility of the offset presence when comparing emission fit and kinematic fit was discussed in [section 4.5](#).

Parameter	Value
FITSFILE	"input file path"
2DFIT	true
NRADII	2
RADSEP	20 (arcsec)
VSYS	0 (km s^{-1})
XPOS	123.63 (px)
YPOS	136.67 (px)
VROT	30 (km s^{-1})
INC	61 ($^{\circ}$)
PA	8.8 ($^{\circ}$)
FREE	VROT VSYS INC PA XPOS YPOS
SIDE	B
WFUNC	2

Table 4.1: Input values of parameters used for the fitting of the MUSE data by 3D-Barolo code. Units of the parameters are in parenthesis (not present in actual file).

Parameter	Value
Vsys	-7.10 (km s^{-1})
Vrot	71.20 (km s^{-1})
P.A.	8.44 ($^{\circ}$)
Incl.	62.06 ($^{\circ}$)
Xcenter	116.92 (px)
Ycenter	135.68 (px)

Table 4.2: Output of the disc fit. Units of the parameters are in parenthesis (not present in actual file).

We also attempted to fit our CO(2-1) moment 1 map, but due to the low spatial resolution and highly perturbed nature of the disc the fit was unreliable.

4.8 Residual velocity map

For the final method of visualization of the ram pressure effect on the molecular disc, we subtracted the rotating disc model of stellar disc obtained in [section 4.7](#) from the velocity field map of the CO data ([Figure 4.3](#)). We used the CO(2-1) map transformed to radial velocities relative to the systematic velocity, as described in [subsection 4.6.4](#). Using

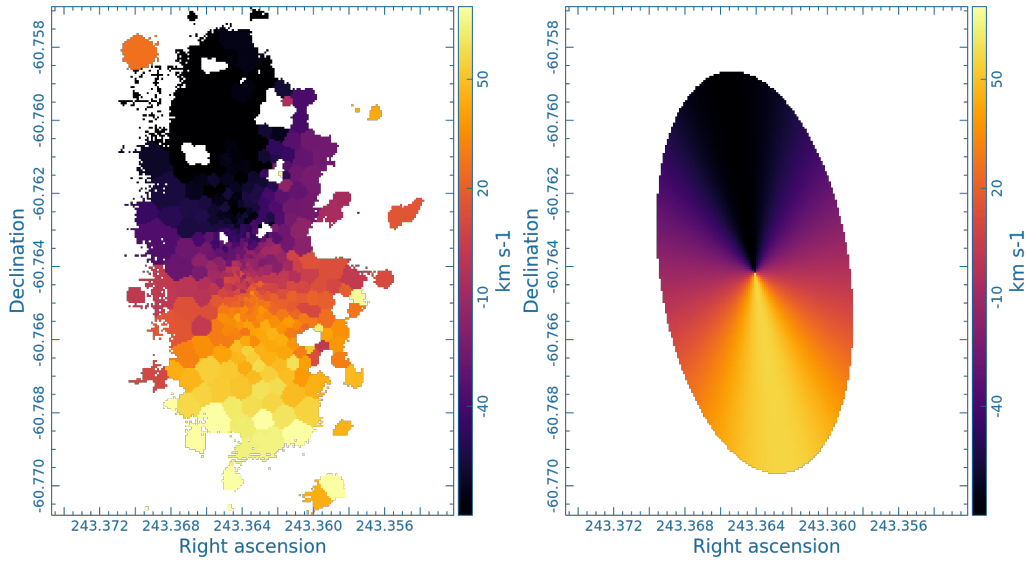


Figure 4.13: Comparison between MUSE data and fitted model, matched scaling

self-written python script, the two maps were spatially matched by comparing pixel coordinates of reference WCS. Values of the overlapping maps were then subtracted, resulting in residual velocity maps depicted in Figure 4.14.

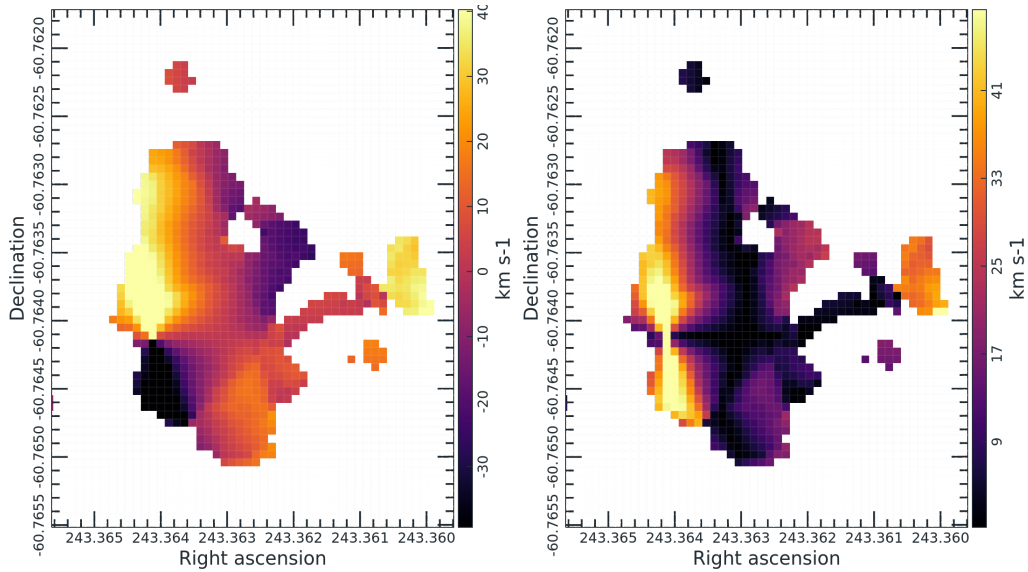


Figure 4.14: Velocity residual map resulting from subtraction of the model of the stellar disc from the ALMA CO velocity map. left: relative deviation from stellar disc, right: absolute deviation

Due to the model characteristics described above (see section 4.7), the resulting images unfortunately show artefacts (symmetrical high deviation along eastern edge) caused by the rapid growth of the velocity. This shows that the used technique was not selected adequately with respect to the position of the molecular disc in close proximity to the center of the stellar disc.

To get better results, more suitable code would need to be used. We decided to substitute the model by the original MUSE data, despite the imperfections in the form of foreground stars and other imperfections. Result of the data subtraction is in [Figure 4.15](#). Two features at offset velocities can be seen in the disc. A red-shifted (offset of about 20 km s^{-1}) feature is located in the southern part of the disc, possibly corresponding to molecular cloud being stripped from the outer regions of the disc. This is consistent with the red-shifted nature of the tail, resulting from the interaction geometry as described above (see [subsection 4.6.4](#)). We can also see the beginning of the tail as the prolonged feature on the right-hand side of the disc, also reaching relatively high deviation from the rotation of the stellar disc. Resulting residual map also contains peculiar blue-shifted (about -35 km s^{-1}) feature in the north-west direction from the center. To uncover origin of this feature, further analysis would be needed (e.g. numerical modeling).

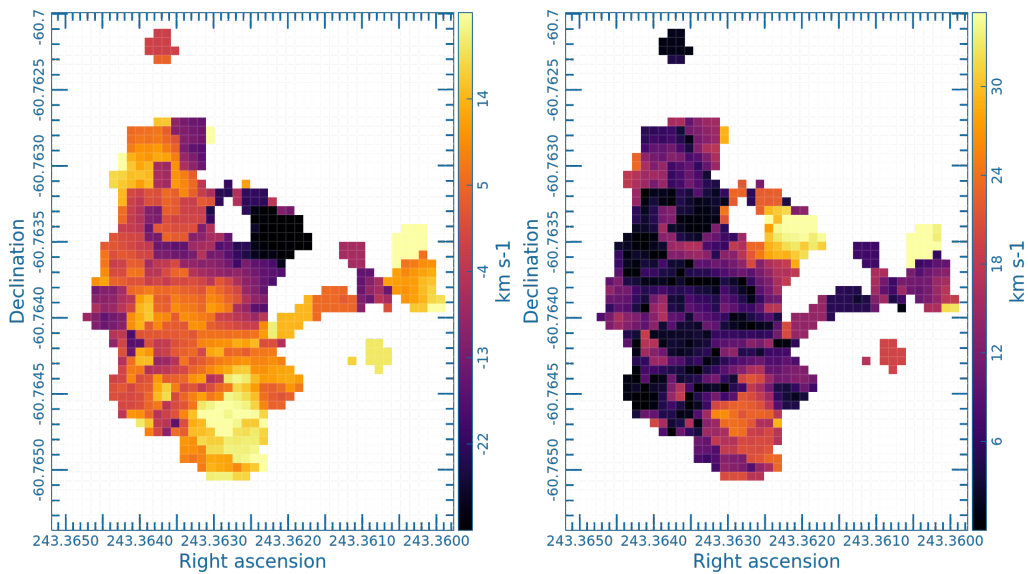


Figure 4.15: Velocity residual map resulting from subtraction of the observed stellar disc velocity map from the ALMA CO velocity map. left: relative deviation from stellar disc, right: absolute deviation

Acknowledgement

This work makes use of the following ALMA data: ADS/JAO.ALMA#2015.1.01520.S, ADS/JAO.ALMA#2015.1.00497.S. ALMA is a partnership of ESO (representing its member states), NSF (USA) and NINS (Japan), together with NRC (Canada), MOST and ASIAA (Taiwan), and KASI (Republic of Korea), in cooperation with the Republic of Chile. The Joint ALMA Observatory is operated by ESO, AUI/NRAO and NAOJ.

Conclusions

In this thesis we focused on learning about Radio-astronomy techniques, Ram-pressure stripping and Data Analysis using either publicly available software or self-written scripts. The target of our analysis was galaxy ESO137-001 located in the southern sky Norma cluster. The galactic interstellar medium is being acted on by the ram-pressure stripping caused by the hydrodynamical interaction with the surrounding intra-cluster medium. We studied the effect by production of position-velocity diagrams and disc modeling.

First three chapters are focused on theoretical introduction to **Radio astronomy**, **Ram pressure stripping** and the observed galaxy **The galaxy ESO137-001**. The fourth chapter (**Data processing**) is focused on the description of methods used for analysis and their results.

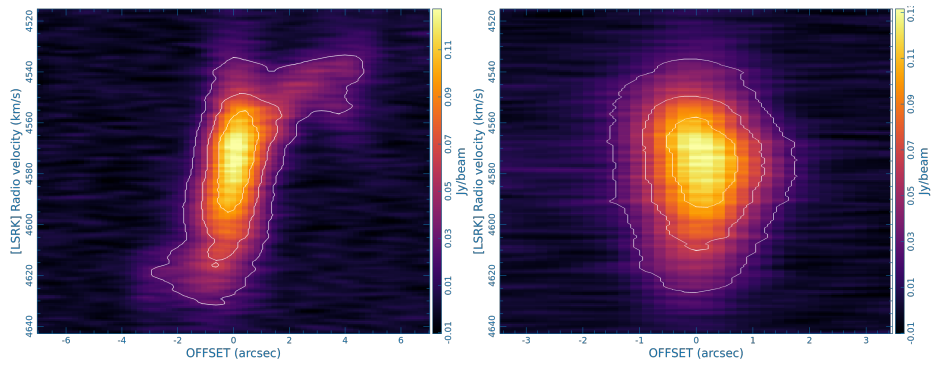
The results of the analysis revealed the severity of ram-pressure stripping activity on the galaxy. Integrated flux map (**Figure 4.3**, left panel) and PVDs along the principal axes (**Figure 4.6**) showed strong asymmetry in the emission distribution. PVD along major axis also showed x-shaped feature that can be attributed to bar structure in the central regions of the galaxy. A strongly asymmetric distribution was further supported by PVDs created along lines parallel with the principal axes (**Figure 4.9** and **Figure 4.10**). Shift of the emission into the north-west direction is consistent with the geometry of the ram-pressure interaction. For comparison we presented PVDs of unperturbed barred galaxy NGC1386 (**Figure 4.8**) and compared the rotation of the molecular disc to the rotation of the unperturbed stellar disc.

For further demonstration of perturbations of the gaseous disc we produced disc model for stellar data-set from MUSE/VLT (**Figure 4.13**), which was then subtracted from our data. However, artifacts of the disc modeling prevented us from further analysis. By substituting the disc model by the original data, we managed to retrieve usable map. The resulting residual velocity map (**Figure 4.15**) clearly shows regions with deviations from the unperturbed stellar disc approaching $\approx 30 \text{ km s}^{-1}$.

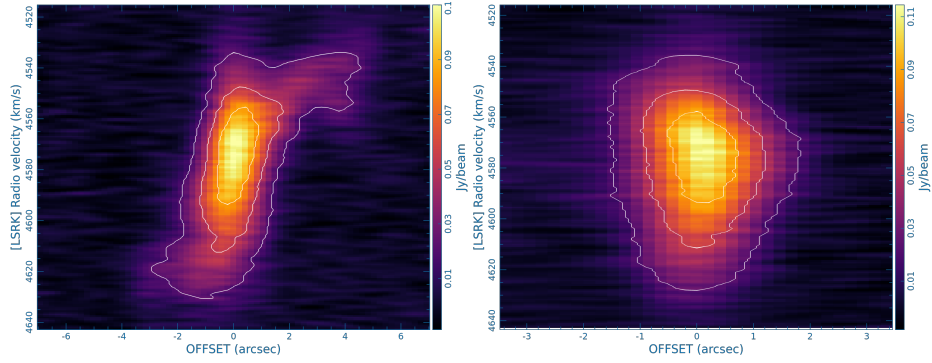
The kinematics of ESO137-001 were mostly unexplored until now. This thesis can be used as reference for similar analysis being done in the future. It can be also extended by incorporation of other existing or newly observed data. New observations of the ESO137-001 and other similar galaxies with modern instruments are already planned. Analysis of these observations can help us uncover yet unknown aspects of the RPS interaction and its affect on the galaxies and their evolution.

Appendix

A Figures - Effect of averaging width on PVD



(a) averaging width 6px



(b) averaging width 10px

Figure 16: Principal axes PVDs with different averaging widths.

B Parallel line region generator function

```

1  import numpy as np
2  from math import pi, sin, cos, radians, acos, asin, degrees
3
4  ## converting arcsec to deg
5  def arcsec_to_deg(arg):
6      out = arg / 3600
7      return out
8
9
10
11 ## converting angle size to WCS angle
12 def offset_to_wcs(offset, ref_coord):
13     '''
14     Converts spatial angle offset to corresponding WCS with
15     spherical trigonometry.
16     approximation: A=B=90, a = b = 90-|dec|, C = d(RA), c
17     = dx
18
19     Input:
20     offset = (dx, dy) ... spatial angle offset ( )
21     ref_coords = (RA0, dec0) ... reference point ( )
22
23     Output:
24     (RA, dec) ... WCS of offset point
25     '''
26
27     # extracting values
28     dx, dy = offset
29     RA0, dec0 = ref_coord
30
31     # getting sign of dx, saving into unit constant 'k'
32     if dx < 0:
33         k = -1
34     else: k = 1
35
36     # calculating side 'a'
37     a = 90 - abs(dec0)
38
39     # calculating output coordinates
40     dec = dec0 + dy
41     RA = RA0 + k * degrees(acos((cos(radians(abs(dx))) - cos(
42         radians(a))**2)/(sin(radians(a))
43         **2)))

```

```
40
41     # assembly of output tuple
42     out = RA, dec
43
44     # returning output values
45     return out
46
47
48
49 ## generating end points coordinates
50 def gen_line_end_points(coord_center, pos_angle, length,
51                        area_width, n_lines = 1):
52     '''
53     Generates coordinates of the linear regions endpoints
54
55     Input:
56     coord_center = (RA_center, dec_center) ... coordinates
57                                     of the line center
58     pos_angle    angle of the line      ... position
59     length       the line ("")         ... length of
60                                     the line ("")
61     area_width   along line to average values ... with of area
62     n_lines      generated lines       ... number of
63
64     Output:
65     end_points = array of shape (n_lines, 5), rows contain:
66                                     [line_index, RA_start, dec_start,
67                                     RA_end, dec_end]
68     '''
69
70     # extracting coordinates
71     RA_center, dec_center = coord_center
72
73     # creating output array, each line in format [
74                                     line_index, x_start, y_start, x_end
75                                     , y_end]
76     end_points = np.zeros((n_lines, 5))
77
78     # creating indexes (-n/2 to n/2)
79     indexes = [x for x in range(int(-n_lines/2), int(
80                                     n_lines/2)+1, 1)]
```

```
74     # writing indexes into 1st element of each line
75     end_points[:,0] = indexes[:]
76
77     # perpendicular distance between lines
78     dist = area_width/(n_lines - 1) # deg
79
80     # coordinates shift between lines
81     dx = dist * cos(radians(pos_angle)) # deg
82     dy = dist * sin(radians(pos_angle)) # deg
83
84     # center_line start and end points in WCS
85     start_offset = [ +(length/2 * sin(radians(pos_angle))),
86                     +(length/2 * cos(radians(pos_angle)
87                                     )))
88
89     center_start_RA , center_start_dec = offset_to_wcs(
90         start_offset , [RA_center ,
91                         dec_center])
92
93     end_offset = [ -(length/2 * sin(radians(pos_angle))), -(
94                    length/2 * cos(radians(pos_angle)))
95                  ]
96
97     center_end_RA , center_end_dec = offset_to_wcs(
98         end_offset , [RA_center , dec_center
99                      ])
100
101     center_start = center_start_RA , center_start_dec
102     center_end = center_end_RA , center_end_dec
103
104     # calculating and saving end points in WCS
105     for i in range(n_lines):
106         if end_points[i, 0] == 0:
107             end_points[i,1:] = center_start + center_end
108
109         else: end_points[i,1:] = offset_to_wcs([-end_points
110                                                [i, 0]*dx, +end_points[i, 0]*dy
111                                                ], center_start) + \
112             offset_to_wcs([-end_points[i,
113                                   0]*dx, +
114                             end_points[
115                                   i, 0]*dy],
116                             center_end)
117
118     # ending generation, returning output array
119     print("End points generated")
120     return end_points
```

```
105
106
107
108 ## function generating region files
109 def gen_parall_lines(coord_center , pos_angle = 0, length =
110                      1, n_lines = 1, \
111                      area_width = 1, output_name = '
112                      line_reg'):
113
114     Generates CASA region files for line regions. Number of
115     lines must be odd to have
116     central line (i=0) going through reference point.
117
118     Input:
119     coord_center = (RA_center , dec_center) ... coordinates
120     of the reference center ( )
121     pos_angle ... position
122     angle of the line ( )
123     length ... length of
124     the line (")
125     area_width ... with of area
126     along line to average values (")
127     n_lines ... number of
128     generated lines
129
130     Output:
131     CASA region files in local directory
132     '''
133
134     # even number of lines control
135     if n_lines % 2 == 0:
136         print("n_lines is not odd number!!!")
137         return
138
139     # getting end pois for lines
140     ends = gen_line_end_points(coord_center , pos_angle ,
141                               arcsec_to_deg(length), \
142                               arcsec_to_deg(area_width),
143                               n_lines)
144
145     print(ends)
146
147     # generating line regions files
148     for i in range(n_lines):
149         # opening (creating) new file
```

```
139     file = open(output_name + str(int(ends[i, 0])), 'w
140                +')
141     # writing first mandatory line
142     file.write('#CRTFv0 CASA Region Text Format version
143                0 \n')
144     # writing line containing data
145     file.write('line [[{}deg, {}deg], [{}deg, {}deg]]
146                coord=ICRS, corr=[I], label="{}
147                _i={}" '.format(ends[i,1], ends
148                [i,2], ends[i,3], ends[i,4],
149                output_name, int(ends[i,0])))
150
151     # closing (saving) file
152     file.close()
153
154     # ending function
155     print("Files generation completed")
156     return
```

C PVD generator function

```

1  import astropy.io.fits as fits
2  import numpy as np
3  from math import sin, cos, radians
4
5
6  ## PVD generator
7  def make_PVD(data, center_coord, PA, length,
8              pixel_increment, Npixel_avg=3):
9      '''
10     Creates PVD along specified line region.
11     Input:
12     data ... data for PVD
13           , axis (x, y)
14     center_coord = (x_center, y_center) ... pixel
15           coordinates of reference point
16     PA ... position
17           angle ( )
18     length ... length of
19           the line (arcsec)
20     coord_increments = (phi, theta) ... spatial
21           angle size of pixels
22     Npixel_avg ... number of
23           pixels to average for PVD value
24     Output:
25     returns 2 arrays - 1st with center offset along line, 2
26     nd with respective according values
27     '''
28
29     # getting shape of input data
30     data_shape = np.shape(data)
31
32     # extracting values from tuples
33     x0, y0 = center_coord
34
35     # length in pixels
36     px_len = round(length/pixel_increment)
37
38     # controlling that number of pixels is odd (=index 0
39     exists)
40
41     if px_len % 2 == 0:
42         px_len +=1

```

```
35
36     # creating indexes
37     indexes = np.arange(-(px_len/2), px_len/2, 1)
38
39     # computing dx, dy increments
40     dx = sin(radians(PA))
41     dy = cos(radians(PA))
42
43     # computing coords along line
44     line_coord = np.zeros((len(indexes), 2))
45
46     for i in range(len(indexes)):
47         line_coord[i] = x0 - indexes[i]*dx, y0 + indexes[i]
48                                     ]*dy
49
50     offset_list = [x*pixel_increment for x in indexes]
51
52     # radial velocities list
53     vR = np.zeros(len(indexes))
54
55     for i in range(len(indexes)):
56
57         # getting list of closest pixels
58         close_pixels = closest_pixels(line_coord[i], PA,
59                                     Npixel_avg)
60
61         # getting average of values from closest pixels
62         Sum = 0
63
64         for coord in close_pixels:
65             # ignoring indexes out of range for axis
66             if coord[0][0] > data_shape[0]-1 or coord[0][1]
67                                     > data_shape[1]-1:
68                 continue
69             if coord[0][0] < 0 or coord[0][1] < 0:
70                 continue
71
72             Sum += data[coord[0][0], coord[0][1]]
73
74         avg = Sum / len(close_pixels)
75         vR[i] = avg
76
77     return offset_list, vR
```

```

77
78
79 ## function assigning closest pixels to PVD line intervals
80 def closest_pixels(coords, line_PA = 0, n_pixels = 1):
81     '''
82     Returns list of indexes of closest pixels
83
84     Input:
85     coords = (x, y) ... pixel coordinates to find closest
86     line_PA ... position angle of the line ( )
87     n_of_pixels ... number of closest pixels to return,
88     integer values only
89
90     Output:
91     pixels = [(x1,y1), ..., (xn, yn)] ... list of px
92     coords of closest pixels
93     '''
94
95     # extracting of ref. coords
96     x0, y0 = coords
97
98     # list to save coords to
99     pixels = []
100
101     # easiest option, closest pixel to ref. coords
102     if int(n_pixels) == 1:
103         x, y = round(x0), round(y0)
104         pixels.append((x,y))
105         return pixels
106
107     # generating perpendicular line
108     line = []
109
110     # indexes
111     N = n_pixels - 1
112     line_ind = np.arange(-N/2, +N/2 + 1)
113
114     # calculating shifts
115     dx = np.cos(radians(line_PA))
116     dy = np.sin(radians(line_PA))
117
118     # calculating line segments
119     for i in line_ind:
120         line.append((x0 + i * dx, y0 + i * dy))

```

```
119  
120     # finding closest pixels to perp. line segments  
121     for i in line:  
122         pixels.append(closest_pixels(i))  
123  
124     return pixels
```

Bibliography

- Athanassoula, E. and M. Bureau (Sept. 1999). “Bar Diagnostics in Edge-on Spiral Galaxies. II. Hydrodynamical Simulations”. In: 522.2, pp. 699–717. DOI: [10.1086/307677](https://doi.org/10.1086/307677). arXiv: [astro-ph/9904206](https://arxiv.org/abs/astro-ph/9904206) [astro-ph].
- Boselli, A., M. Fossati, and M. Sun (Sept. 2021). “Ram Pressure Stripping in High-Density Environments”. In: *arXiv e-prints*, arXiv:2109.13614, arXiv:2109.13614. arXiv: [2109.13614](https://arxiv.org/abs/2109.13614) [astro-ph.GA].
- Burke, Bernard F., Francis Graham-Smith, and Peter N. Wilkinson (2019). “Aperture Synthesis”. In: *An Introduction to Radio Astronomy*. 4th ed. Cambridge University Press, pp. 220–265. DOI: [10.1017/9781316987506.013](https://doi.org/10.1017/9781316987506.013).
- Chung, Aeree et al. (Dec. 2009). “VLA Imaging of Virgo Spirals in Atomic Gas (VIVA). I. The Atlas and the H I Properties”. In: 138.6, pp. 1741–1816. DOI: [10.1088/0004-6256/138/6/1741](https://doi.org/10.1088/0004-6256/138/6/1741).
- Cowie, L. L. and A. Songaila (Apr. 1977). “Thermal evaporation of gas within galaxies by a hot intergalactic medium”. In: 266, pp. 501–503. DOI: [10.1038/266501a0](https://doi.org/10.1038/266501a0).
- Di Teodoro, E. M. and F. Fraternali (Aug. 2015). “^{3D} BAROLO: a new 3D algorithm to derive rotation curves of galaxies”. In: 451.3, pp. 3021–3033. DOI: [10.1093/mnras/stv1213](https://doi.org/10.1093/mnras/stv1213). arXiv: [1505.07834](https://arxiv.org/abs/1505.07834) [astro-ph.GA].
- Dressler, A. (Mar. 1980). “Galaxy morphology in rich clusters: implications for the formation and evolution of galaxies.” In: 236, pp. 351–365. DOI: [10.1086/157753](https://doi.org/10.1086/157753).
- Ebeling, H., L. N. Stephenson, and A. C. Edge (Feb. 2014). “Jellyfish: Evidence of Extreme Ram-pressure Stripping in Massive Galaxy Clusters”. In: 781.2, L40, p. L40. DOI: [10.1088/2041-8205/781/2/L40](https://doi.org/10.1088/2041-8205/781/2/L40). arXiv: [1312.6135](https://arxiv.org/abs/1312.6135) [astro-ph.GA].
- Gunn, James E. and III Gott J. Richard (Aug. 1972). “On the Infall of Matter Into Clusters of Galaxies and Some Effects on Their Evolution”. In: 176, p. 1. DOI: [10.1086/151605](https://doi.org/10.1086/151605).
- Jáchym, Pavel, Françoise Combes, et al. (Sept. 2014). “Abundant Molecular Gas and Inefficient Star Formation in Intracluster Regions: Ram Pressure Stripped Tail of the Norma Galaxy ESO137-001”. In: 792.1, 11, p. 11. DOI: [10.1088/0004-637X/792/1/11](https://doi.org/10.1088/0004-637X/792/1/11). arXiv: [1403.2328](https://arxiv.org/abs/1403.2328) [astro-ph.GA].
- Jáchym, Pavel, Jeffrey D. P. Kenney, et al. (Oct. 2019). “ALMA Unveils Widespread Molecular Gas Clumps in the Ram Pressure Stripped Tail of the Norma Jellyfish Galaxy”. In: 883.2, 145, p. 145. DOI: [10.3847/1538-4357/ab3e6c](https://doi.org/10.3847/1538-4357/ab3e6c). arXiv: [1905.13249](https://arxiv.org/abs/1905.13249) [astro-ph.GA].
- Luo, Rongxin and collective (in prep., 2022). “Tracing the kinematics of the whole ram pressure stripped tails in ESO137-001”.

- Marr, Jonathan M., Ronald Lee Snell, and Stanley Kurtz (2021). “Aperture synthesis”. In: *Fundamentals of Radio Astronomy*. CRC Press, pp. 181–280.
- Massardi, M. et al. (Aug. 2021). “The Additional Representative Images for Legacy (ARIL) Project for the ALMA Science Archive”. In: 133.1026, 085001, p. 085001. DOI: [10.1088/1538-3873/ac159c](https://doi.org/10.1088/1538-3873/ac159c). arXiv: [2107.11071](https://arxiv.org/abs/2107.11071) [astro-ph.IM].
- Montes, Mireia (Dec. 2019). “The intracluster light and its role in galaxy evolution in clusters”. In: *arXiv e-prints*, arXiv:1912.01616, arXiv:1912.01616. arXiv: [1912.01616](https://arxiv.org/abs/1912.01616) [astro-ph.GA].
- Skrutskie, M. F. et al. (Feb. 2006). “The Two Micron All Sky Survey (2MASS)”. In: 131.2, pp. 1163–1183. DOI: [10.1086/498708](https://doi.org/10.1086/498708).
- Sun, M., M. Donahue, E. Roediger, et al. (Jan. 2010). “Spectacular X-ray Tails, Intracluster Star Formation, and ULXs in A3627”. In: 708.2, pp. 946–964. DOI: [10.1088/0004-637X/708/2/946](https://doi.org/10.1088/0004-637X/708/2/946). arXiv: [0910.0853](https://arxiv.org/abs/0910.0853) [astro-ph.CO].
- Sun, M., M. Donahue, and G. M. Voit (Dec. 2007). “H α Tail, Intracluster H II Regions, and Star Formation: ESO 137-001 in Abell 3627”. In: 671.1, pp. 190–202. DOI: [10.1086/522690](https://doi.org/10.1086/522690). arXiv: [0706.1220](https://arxiv.org/abs/0706.1220) [astro-ph].
- Sun, M., C. Jones, et al. (Feb. 2006). “A 70 Kiloparsec X-Ray Tail in the Cluster A3627”. In: 637.2, pp. L81–L84. DOI: [10.1086/500590](https://doi.org/10.1086/500590). arXiv: [astro-ph/0511516](https://arxiv.org/abs/astro-ph/0511516) [astro-ph].
- Sun, Ming et al. (Dec. 2021). “A universal correlation between warm and hot gas in the stripped tails of cluster galaxies”. In: *Nature Astronomy* 6, pp. 270–274. DOI: [10.1038/s41550-021-01516-8](https://doi.org/10.1038/s41550-021-01516-8). arXiv: [2103.09205](https://arxiv.org/abs/2103.09205) [astro-ph.GA].
- Vollmer, B. et al. (Nov. 2001). “Ram Pressure Stripping and Galaxy Orbits: The Case of the Virgo Cluster”. In: 561.2, pp. 708–726. DOI: [10.1086/323368](https://doi.org/10.1086/323368). arXiv: [astro-ph/0107237](https://arxiv.org/abs/astro-ph/0107237) [astro-ph].
- Woudt, P. A., R. C. Kraan-Korteweg, and A. P. Fairall (Dec. 1999). “Extragalactic large-scale structures behind the southern Milky Way. III. Redshifts obtained at the SAAO in the Great Attractor region”. In: 352, pp. 39–48. arXiv: [astro-ph/9911274](https://arxiv.org/abs/astro-ph/9911274) [astro-ph].
- Zabel, Nikki et al. (Feb. 2019). “The ALMA Fornax Cluster Survey I: stirring and stripping of the molecular gas in cluster galaxies”. In: 483.2, pp. 2251–2268. DOI: [10.1093/mnras/sty3234](https://doi.org/10.1093/mnras/sty3234). arXiv: [1811.11759](https://arxiv.org/abs/1811.11759) [astro-ph.GA].